Design of a multivalent bifunctional chelator for diagnostic ^{64}Cu PET imaging in Alzheimer's disease

Hong-Jun Cho[a], Truc T. Huynh[b,c], Buck E. Rogers[b], and Liviu M. Mirica[a,d,1]

[a]Department of Chemistry, University of Illinois at Urbana–Champaign, Urbana, IL 61801; [b]Department of Radiation Oncology, Washington University School of Medicine, St. Louis, MO 63108; [c]Department of Chemistry, Washington University, St. Louis, MO 63130; and [d]Hope Center for Neurological Disorders, Washington University School of Medicine, St. Louis, MO 63110

Edited by Joan Selverstone Valentine, University of California, Los Angeles, CA, and approved October 27, 2020 (received for review July 5, 2020)

Herein, we report a ^{64}Cu positron emission tomography (PET) imaging agent that shows appreciable in vivo brain uptake and exhibits high specific affinity for beta-amyloid (Aβ) aggregates, leading to the successful PET imaging of amyloid plaques in the brains of 5xFAD mice versus those of wild-type mice. The employed approach uses a bifunctional chelator with two Aβ-interacting fragments that dramatically improves the Aβ-binding affinity and lipophilicity for favorable blood–brain barrier penetration, while the use of optimized-length spacers between the Cu-chelating group and the Aβ-interacting fragments further improves the in vivo Aβ-binding specificity and brain uptake of the corresponding ^{64}Cu PET imaging agent.

Alzheimer's disease | positron emission tomography imaging | blood–brain barrier | amyloid beta (Aβ) peptide | multivalent effect

Alzheimer's disease (AD) is the most common neurodegenerative disease resulting in cognitive impairment, memory loss, and physical disability. The major neuropathological hallmark of AD is the deposition of extracellular amyloid plaques consisting of the beta-amyloid (Aβ) peptide (1, 2), and more recently the smaller, soluble Aβ oligomers have been shown to be involved in the synapse loss and neuronal injury occurring prior to the onset of AD (3–6).

Before the development of the first positron emission tomography (PET) imaging agent Pittsburgh Compound B for the detection of amyloid plaques in humans (7, 8), a conclusive AD diagnosis relied on postmortem examination of the brain (9, 10). More recently, the Food and Drug Administration has approved three ^{18}F PET imaging agents as Aβ probes for AD diagnosis (10–15). However, all these PET imaging agents use short-lived radioisotopes such as ^{11}C ($t_{1/2}$ = 20.4 m) and ^{18}F ($t_{1/2}$ = 109.8 m), which limit their widespread use (16). By contrast, the ^{64}Cu radionuclide has a longer half-life ($t_{1/2}$ = 12.7 h), exhibits well-established coordination chemistry (17), and various ^{64}Cu complexes were successfully used in vivo for the PET imaging and diagnosis of various tumors (18–20) and hypoxia (21–23). While recent studies have focused on the development of Aβ-interacting ^{64}Cu PET imaging agents that have shown Aβ-binding properties in vitro and ex vivo (13, 15, 24–28), there is still a need to develop compounds that exhibit high affinity toward Aβ aggregates, are strong chelators capable of forming ^{64}C -complexes that are stable in vivo, and ultimately can cross the blood–brain barrier (BBB) for efficient PET imaging.

Previously we have reported Aβ-targeting bifunctional chelators (BFCs) for potential therapeutic and PET imaging applications (29–34). Herein, we report compounds containing Aβ-interacting fragments and a metal-chelating group designed based on a multivalent ligand approach and variable-length spacer strategy, which to the best of our knowledge have not been used for any radiometal PET neuroimaging agent development. Multivalent ligands commonly bind to receptors with improved affinity vs. the monovalent derivatives (35–37). In addition, the lipophilicity of the multivalent BFCs can be optimized by varying the length and type of the molecular spacer (38, 39), which can also separate the Aβ-interacting and the metal-chelating groups (40, 41). The beneficial effects of the multivalent BFCs and use of an optimal spacer employed herein leads to the successful development of a promising ^{64}Cu PET imaging agent for the detection of amyloid aggregates in 5xFAD mice vs. wild-type (WT) mice.

Results and Discussion

The targeted BFCs consist of three parts: an Aβ-interacting fragment, a metal-chelating group, and a spacer (Scheme 1). For the Aβ-interacting fragment we chose the 2-(2-formyl-5-furanyl)-3-hydroxymethylbenzofuran moiety that was shown to bind to soluble Aβ species in vitro and in vivo (42). Importantly, this molecular structure has not been used previously for developing ^{64}Cu-based PET imaging agents for the Aβ aggregates relevant to AD. A well-known strong Cu chelator, 1,4,7-triazacyclononane-1,4,7-triacetic acid (NOTA), was used due to its efficient ^{64}Cu radiolabeling and in vivo stability (43, 44), and the two molecular fragments were linked with ethyl, butyl, hexyl, or ethylene glycol spacers. The synthesis of the BFCs started with 3-methylbenzofuran that was brominated for further conjugation (*SI Appendix*, Scheme S1). The four spacers were then connected at the 3-bromomethylbenzofuran position, followed by Suzuki coupling with 5-formyl-2-furanylboronic acid at the 2-bromobenzofuran position. After Boc group deprotection, the Aβ-interacting fragments containing the different linkers were coupled to NOTA through sequential amide coupling to generate the monovalent and divalent BFCs **6a–6d** and **7a–7d**, respectively (Scheme 1). The NOTA-conjugated

Significance

Metal radiotracers exhibit beneficial properties that can improve in vivo positron emission tomography (PET) imaging over traditional radionuclides, such as longer half-lives, facile last-stage radiolabeling steps, and the potential for dual imaging-therapy applications. Among such radionuclides, ^{64}Cu exhibits a longer half-life ($t_{1/2}$ = 12.7 h) that allows for later PET imaging times and the ability to distribute ^{64}Cu imaging agents to facilities that do not have an on-site cyclotron. Herein, we report a ^{64}Cu PET imaging agent that shows appreciable in vivo brain uptake and exhibits high specific affinity for beta-amyloid aggregates, leading to the successful PET imaging of amyloid plaques in the brains of 5xFAD mice versus those of wild-type mice.

Author contributions: H.-J.C., B.E.R., and L.M.M. designed research; H.-J.C. and T.T.H. performed research; H.-J.C. and T.T.H. analyzed data; and H.-J.C., T.T.H., B.E.R., and L.M.M. wrote the paper.

The authors declare no competing interest.

This article is a PNAS Direct Submission.

Published under the PNAS license.

[1]To whom correspondence may be addressed. Email: mirica@illinois.edu.

This article contains supporting information online at https://www.pnas.org/lookup/suppl/doi:10.1073/pnas.2014058117/-/DCSupplemental.

First published November 24, 2020.

Downloaded at Palestinian Territory, occupied on November 23, 2021

www.manaraa.com

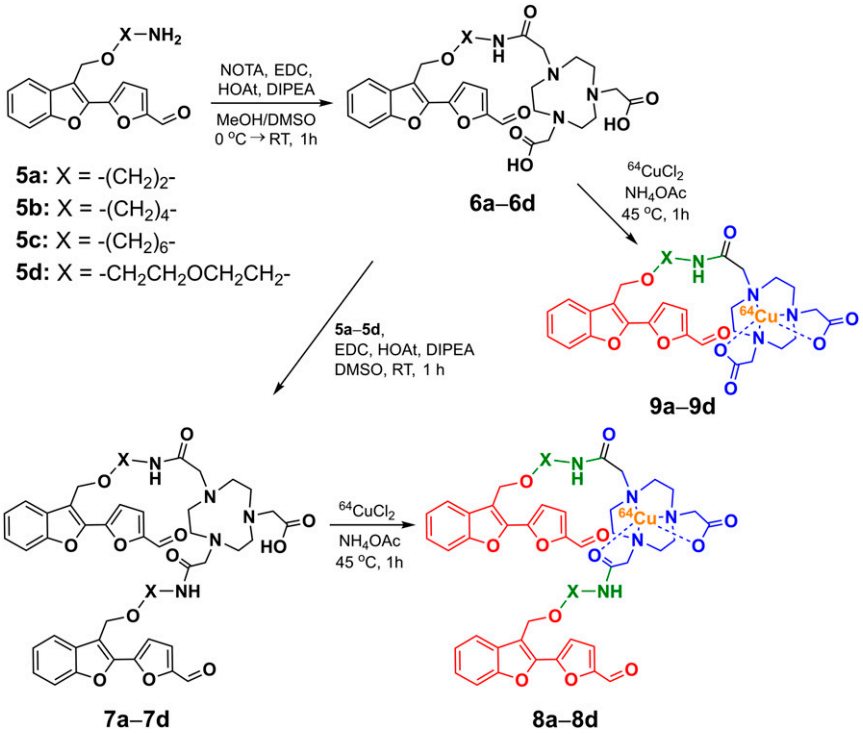

Scheme 1. Synthetic route and structures of the ^{64}Cu-complexes **8a–8d** and **9a–9d**. The metal-binding, spacer, and Aβ-interacting fragments are shown in blue, green, and red, respectively.

compounds were then labeled with $^{64}CuCl_2$ in NH_4OAc (pH 5.5) and the ^{64}Cu-complexes (**8a–8d**) were used without further purification (radiochemical yield >95%, *SI Appendix*, Fig. S1). The ^{64}Cu complexes **9a–9d** of the monovalent BFCs **6a–6d** were also synthesized and used for log D value determination.

To evaluate the affinity of these compounds toward amyloid plaques, we treated brain sections from 3-mo-old 5xFAD mice with the nonradioactive Cu complexes **8a′–8d′**. Since the Cu complexes have intrinsic fluorescence from the Aβ-interacting fragment without significant Cu-mediated fluorescence quenching (*SI Appendix*, Fig. S2), the brain section staining shows that **8a′–8d′** bind specifically to the amyloid plaques. This was confirmed by subsequent immunostaining with the AF594-conjugated HJ3.4 antibody (AF594-HJ3.4) that binds to a range of Aβ species (10–15), suggesting that the Cu complexes could detect the native Aβ aggregates ex vivo (Fig. 1 and *SI Appendix*, Fig. S3). Among the different Cu complexes, **8b′**and **8c′** exhibit vivid signals and strong colocalization with the AF594-HJ3.4 antibody (Pearson's correlation coefficients: 0.65 for **8b′**, 0.59 for **8c′**) (45).

We then performed ex vivo autoradiography studies to quantitatively evaluate the specificity of ^{64}Cu-complexes **8a–8d** toward Aβ aggregates using wild-type (WT) and 5xFAD mouse brain sections. After incubating the brain sections with the ^{64}Cu-complexes, the signal intensity for the different brain sections was determined using phosphor imaging autoradiography. For the blocking studies, the brain sections were pretreated with the nonradioactive Aβ-interacting molecule 2-(2-formyl-5-furanyl)-3-hydroxymet-hylbenzofuran as a blocking agent (42). Whereas the WT brain sections treated with **8a–8d** showed minimal radioactive intensity, the signal intensity was significantly higher for the 5xFAD brain sections treated with **8a–8d** (Fig. 2*A*), indicative of specific binding of **8a–8d** to the Aβ aggregates. Among them, **8b** and **8c** showed dramatic autoradiography contrast in the 5xFAD mouse brain sections vs. the WT mouse brain sections, leading to high 5xFAD to WT intensity ratios of 4.6 for **8b** and 4.1 for **8c**, respectively (Fig. 2*B*). Furthermore, the measured specific activity sharply decreased in the 5xFAD mouse brain sections pretreated with the blocking agent to levels comparable to those observed for the WT brain sections (Fig. 2*B*), further confirming that **8a–8d** bind specifically to Aβ aggregates with negligible nonspecific binding to other biomolecules present in the brain tissue.

In order to confirm the multivalent ligand effect on the binding affinity toward Aβ aggregates, we compared the autoradiography images of the 5xFAD mouse brain sections incubated with the divalent (**8b–8c**) vs. the monovalent (**9b–9c**) compounds. As anticipated, the signal intensities of the divalent compounds were higher than those of the monovalent compounds, with signal intensity ratios of 1.5 (**8b**: **9b**) and 1.6 (**8c**: **9c**), respectively (*SI Appendix*, Fig. S4). These results support the multivalent strategy in our BFC design for Aβ binding, with the divalent BFCs amplifying the radioactive intensity in the AD brains.

We have also investigated the lipophilicity of **8a–8d** to predict their BBB permeability by measuring the octanol–phosphate-buffered saline (PBS) partition coefficient (log D) (46). The BFCs were more lipophilic as the alkyl spacer length increased, while the ethylene glycol linker exhibited slightly lower lipophilicity [ethylene glycol (**d**) ~ ethyl (**a**) < butyl (**b**) < hexyl (**c**), Fig. 2*C*]. This trend was observed in both divalent (**8a–8d**) and monovalent (**9a–9d**) BFCs, and is also correlated with the retention times observed for each ^{64}Cu-complex by radio-high performance liquid chromatography (radio-HPLC) (*SI Appendix*, Fig. S1). Furthermore, the divalent compounds were more lipophilic than the monovalent compounds, likely due to the two hydrophobic Aβ-interacting fragments and one carboxylate group in the divalent molecules vs. the monovalent compound with one Aβ-interacting fragment and two carboxylate groups. In particular, the log D values of **8a–8d** were in the optimal range of

Downloaded at Palestinian Territory, occupied on November 23, 2021
www.manaraa.com

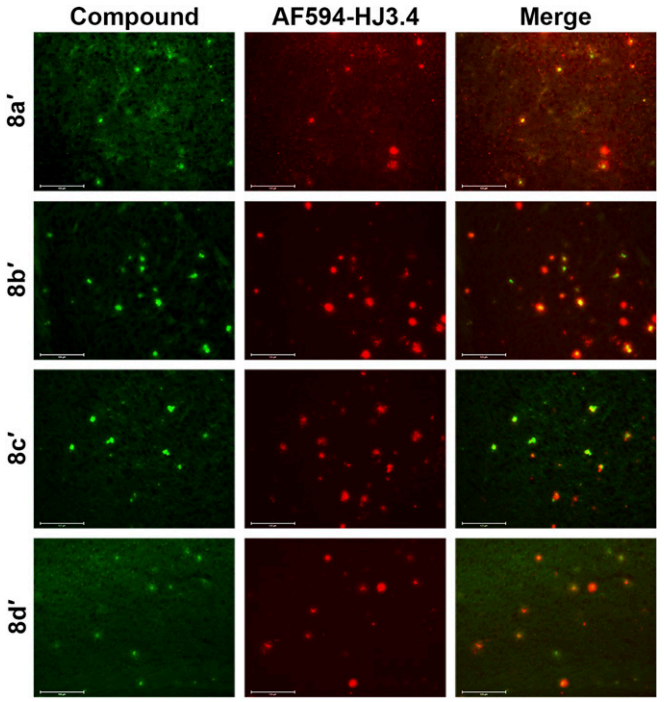

Fig. 1. Fluorescence microscopy images of 5xFAD mice brain sections incubated with nonradioactive Cu complexes of (**8a**′–**8d**′). The fluorescence signals from the Cu complexes and AF594-HJ3.4 antibody were monitored under green and red channels, respectively. (Scale bar, 125 μm.) The compounds were appreciably colocalized with the amyloid plaques immunostained with AF594-HJ3.4 (Pearson's R correlation coefficients, **8a**′: 0.45; **8b**′: 0.65; **8c**′: 0.59; **8d**′: 0.46).

lipophilicity for a central nervous system drug (–0.5 ≤ log D ≤ 3.8, median value: 1.7) (47), being potentially suitable for brain imaging in in vivo applications. Therefore, the multivalent strategy in the BFC design significantly improves their lipophilicity to be favorable for BBB penetration, and this lipophilicity can be further controlled by the spacer linking the Aβ-interacting fragment(s) and the Cu-chelating group.

Before employing the developed compounds in in vivo studies, we have evaluated the cytotoxicity of the nonradioactive Cu complexes **8a**′–**8d**′ using neuroblastoma Neuro-2a cells and the Cell Counting Kit-8 assay. Encouragingly, all compounds exhibited no cytotoxicity up to 10 μM (*SI Appendix*, Fig. S5), and thus these compounds are not expected to be toxic at the concentrations (<6 μM) employed in imaging applications. Next, we investigated the brain uptake and in vivo biodistribution of the ^{64}Cu complexes **8a**–**8d** in WT mice (CD-1). The radioactive **8a**–**8d** were administered into the CD-1 mice via intravenous injection, and the radioactivity accumulated in each organ was determined at 2-, 60-, and 240-min postinjection (*SI Appendix*, Figs. S6 and S7 and Table S1). Overall, high initial uptake in each organ was observed, followed by a clearance of ∼75% of ^{64}Cu after 4 h and along with an increase in the brain to blood ratio. Interestingly, **8c**, the most lipophilic compound in the series, was trapped mostly in the lung, with an appreciable accumulation of the radioactivity even after 4 h and leading to poor brain uptake (Fig. 2*D*). Excitingly, **8b** and **8d** exhibited higher brain uptake at 2 and 60 min, with low nonspecific accumulation in the major organs (Fig. 2*D*). Taken together, these studies strongly suggest that **8b** and **8d** exhibit specific Aβ binding and high BBB penetration and thus are promising candidates for Aβ detection in vivo.

Positron Emission Tomography – Computed Tomography (PET/CT) imaging studies were then performed with age-matched WT and 5xFAD mice (n = 3 for each group), and the images were acquired from the dynamic scans for 30 min after intravenous injection of **8b** and **8d** (∼3-MBq doses). The axial, coronal, and sagittal PET images show that the WT mouse brains exhibit lower intensity than the 5xFAD mouse brains (Fig. 3*A* and *SI Appendix*, Fig. S8). Quantitative time–activity curves clearly reveal higher brain retention of **8b** and **8d** in the 5xFAD mice than those in the WT mice, with 35% higher signal intensity for **8b** and 26% for **8d** after 30 min, respectively (Fig. 3 *B* and *C*). In particular, a statistically significant (P = 0.0203) higher brain uptake was observed for **8b** in the 5xFAD mice vs. the WT mice after 4.5 min postinjection, whereas a P = 0.0699 value was obtained for the 5xFAD mice vs. the WT mice treated with **8d** (Fig. 3*D*). Overall, we conclude that the improved PET imaging contrast for **8b** is attributable to its higher BBB permeability and Aβ-binding ability, with minimal nonspecific binding in the brain.

After the PET/CT scans, the brain uptake for **8b** and **8d** were quantified using a postimaging biodistribution study, followed by brain sectioning for autoradiography. Consistent with the PET imaging data, **8b** provided a statistically significantly higher brain uptake (P = 0.0269) in the 5xFAD mice vs. the WT mice (Fig. 3*E* and *SI Appendix*, Fig. S9), while a larger brain-to-blood specific activity ratio was also observed for the 5xFAD vs. the WT mice injected with **8b** (*SI Appendix*, Fig. S10). Furthermore, the signal intensity for **8b** and **8d** in the autoradiography studies was clearly higher in the brain sections of the 5xFAD mice vs. those of the WT mice (*SI Appendix*, Fig. S11), suggesting that **8b** and **8d** can penetrate the BBB and accumulate specifically within the amyloid plaques in the brains of 5xFAD mice.

Conclusions

In conclusion, we have synthesized a series of bifunctional chelators using a multivalent ligand approach and variable spacer strategy.

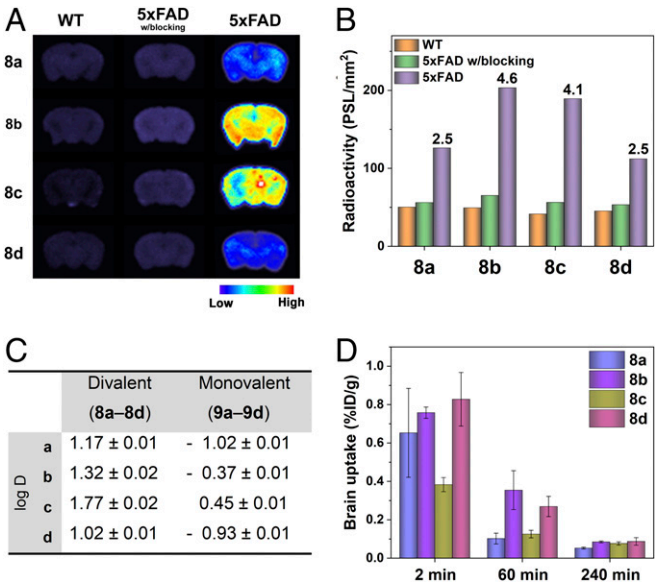

Fig. 2. (*A*) Autoradiography images of the brain sections from WT and 5xFAD mice after treatment with **8a**–**8d** in the absence or presence of a blocking agent. (*B*) Average radioactivity of the brain sections in the autoradiography images. The numbers in the bar graph are the intensity ratios of 5xFAD to WT in each group. (*C*) Distribution coefficients (log D) of **8a**–**8d** and **9a**–**9d** in octanol/PBS (pH 7.4). (*D*) Brain uptake (% ID/g) results from the in vivo biodistribution studies in CD-1 mice at 2-, 60-, and 240-min postinjection of **8a**–**8d**.

Downloaded at Palestinian Territory, occupied on November 23, 2021
www.manaraa.com

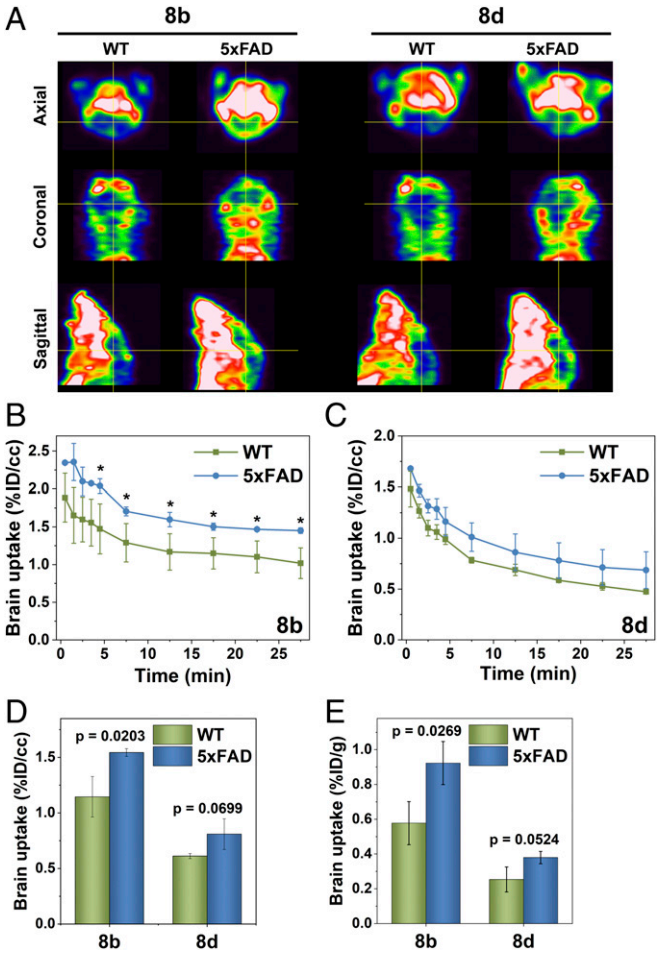

Fig. 3. (*A*) Representative axial, coronal, and sagittal PET images of **8b** and **8d** in WT and 5xFAD mice with dynamic scans summed from 7.5- to 27.5-min postinjection. The cross-hair shows the brain area in the mice. Mean brain uptake time–activity curves for (*B*) **8b** and (*C*) **8d**, generated from the dynamic micro-PET images. (*D*) Mean brain uptake (t = 7.5–27.5-min postinjection) obtained from the dynamic PET images. (*E*) Brain uptake (% ID/g) results from the post-PET biodistribution studies in WT and 5xFAD mice. Error bars represent SDs (n = 3 mice), and the statistical analysis was evaluated according to one-way ANOVA (*P < 0.05, or specific P values are included).

The multivalent effect enhances not only the binding affinity toward Aβ species but also the lipophilicity for favorable BBB penetration, which is also controlled by the spacer used between the Aβ-targeting and the metal-chelating fragments. Based on the in vitro and biodistribution results, the ^{64}Cu complexes **8b** and **8d** were selected for further in vivo PET imaging, providing high Aβ specificity and appreciable brain uptake with minimal nonspecific adsorption in the brain. Excitingly, **8b** exhibited statistically significant higher brain retention in the 5xFAD mice versus the WT mice, thus holding potential as a diagnostic PET imaging agent for AD. Overall, the employed approach based on multivalent and spacer molecular design can be applied to other ^{64}Cu-based diagnostic PET imaging applications in neurodegenerative disorders.

Methods and Materials

The general experimental methods, chemical synthesis details, and additional results are described in *SI Appendix*.

Mouse Brain Section Staining Analysis. All animal studies were performed with the approval of the Institutional Animal Care and Use Committee of the University of Illinois at Urbana–Champaign and Washington University School of Medicine. To obtain mouse brain sections, 5xFAD transgenic mice (3 and 6-mo-old) were euthanized under deep anesthesia for perfusion and brain harvesting. The mice were anesthetized with isoflurane and perfused transcardially with heparinized PBS followed by brain collection. Mouse brain tissues were fixed in 4% paraformaldehyde at 4 °C overnight and then preserved in 30% sucrose (wt/vol) in PBS (pH 7.4) at 4 °C for 3 d. The brains were coronally sectioned (thickness: 50 μm) on a freezing sliding microtome. The free-floating brain sections were kept in a cryoprotectant solution of 30% ethylene glycol (vol/vol) and 15% sucrose (wt/vol) in 0.1 M phosphate buffer (pH 7.4) at –20 °C. The brain sections from age-matched WT mice were also obtained following the same procedure. For brain staining experiment, the brain sections from 3-mo-old 5xFAD mice were permeabilized in PBS with 0.25% Triton-X100 for 30 min at room temperature and washed with PBS (3 × 5 min). The brain sections were treated with premixed solutions containing 25 μM of the compounds (**7a**–**7d**) and 25 μM of $CuCl_2$ in PBS for 1 h. After sequential washes with PBS (1 × 5 min), 50% EtOH/PBS (1 × 5 min), and PBS (3 × 5 min), the brain sections were treated with blocking solution (0.1% Triton-X100, 0.2% dry milk, and 1% BSA in PBS) at room temperature for 1 h, and then incubated with AF594-conjugated anti-Aβ antibody (AF594-HJ3.4 antibody) solution (1:1,000 dilution in blocking solution) at room temperature for 1 h. After washing with PBS (1 × 5 min), the brain sections were mounted with mounting media. Fluorescence images were visualized using an Invitrogen EVOS FL Auto 2 Imaging System equipped with excitation (470/22, 585/29 nm) and emission (510/42, 624/40 nm) light cubes for green and red channels, respectively. Colocalization analysis and determination of the Pearson's correlation coefficient was performed with the imaging software Fiji (ImageJ 1.52p).

Radiolabeling Studies. ^{64}Cu was produced by a (p,n) reaction on enriched ^{64}Ni on a CS-15 biomedical cyclotron (Cyclotron Corporation) at Mallinckrodt Institute of Radiology, Washington University School of Medicine, and purified with an automated system using standard procedures (48, 49). A stock solution of $^{64}CuCl_2$ was diluted with a 10-fold excess of 0.1 M ammonium acetate (NH_4OAc) buffer (pH 5.5). Typical labeling of compounds was achieved by adding 20 μL of compound solutions (**6a**–**6d** or **7a**–**7d**, 1 mM) in dimethyl sulfoxide (DMSO) into 7.4 MBq (200 μCi) of $^{64}CuCl_2$ in 100 μL of 0.1 M NH_4OAc (pH 5.5). The reactions were incubated on a thermomixer with 800-rpm agitation at 45 °C for 30 min. Radiolabeled compounds were analyzed by high-performance HPLC, with water (0.1% TFA) and acetonitrile (0.1% TFA) mobile phase with a gradient of 0–100% acetonitrile over 12 min with a flow rate of 1 mL/min. Divalent ^{64}Cu-labeled complexes (**8a**–**8d**) and monovalent ^{64}Cu-labeled complexes (**9a**–**9d**) were obtained in high radiochemical yield (> 95%) and therefore used without further purification.

Octanol/PBS Partition Coefficient (Log D) Measurements. The ^{64}Cu-labeled complexes (**8a**–**8d** and **9a**–**9d**) (6–8 μL, 0.37 MBq, 10 μCi) were added to a mixture of 0.5 mL of PBS (pH 7.4) and 0.5 mL of 1-octanol. The mixtures were vortexed at 1,000 rpm for 1 h and then given 30 min for the layers to separate. Aliquots (100 μL) were withdrawn from the aqueous and 1-octanol layers and counted separately in an automated gamma counter. The partition coefficients were calculated based on the equation of log D = log ($[M]_{oct}/[M]_{aq}$). The experiment was conducted in triplicates of triplicates, and the overall average was recorded as the final log D value for each complex.

Autoradiography Studies. Free-floating brain sections from 6-mo-old 5xFAD and aged-matched WT mice were washed with PBS (3 × 5 min) and incubated with 1.48 MBq (40 μCi) of ^{64}Cu-labeled complexes (**8a**–**8d**) in 2 mL of PBS at room temperature for 1 h. After the incubation, the brain sections were washed with PBS (3 × 5 min), and then were transferred onto glass slides and dried under an air stream. The slides were mounted onto a phosphor imaging screen plate (GE Healthcare Life Sciences) and exposed overnight at –20 °C. The plates were scanned on a Typhoon FLA 9500 biomolecular imager (GE Healthcare) at a 25-μm resolution, and the resulting images were processed and quantified using ImageQuant TL 8.1 (GE Healthcare) and ImageJ (1.52p). The radioactivity of the autoradiographed brain sections was determined as photostimulated luminescence per unit area (mm^3). For blocking experiments, the 5xFAD brain sections were incubated with 100 equiv. of the nonradiolabeled compound, 2-(2-formyl-5-furanyl)-3-hydroxymethylbenzofuran (42) for 10 min and then with ^{64}Cu-labeled complexes (**8a**–**8d**) under the same conditions. For comparison experiments between divalent and monovalent compounds, the 5xFAD brain

Downloaded at Palestinian Territory, occupied on November 23, 2021

www.manaraa.com

sections were incubated with ^{64}Cu-labeled complexes (divalent: **8b** and **8c**, monovalent: **9b** and **9c**) under the same conditions.

Biodistribution Studies. All animal experiments were performed in compliance with the Guidelines for Care and Use of Research Animals established by the Division of Comparative Medicine and the Animal Studies Committee of the University of Illinois at Urbana–Champaign and Washington University School of Medicine. Biodistribution studies were conducted in WT CD-1 female mice (Charles River Laboratories) of age 5–7 wk weighing 25.1 ± 1.4 g. The mice were injected with 0.22–0.37 MBq (6–10 μCi) of ^{64}Cu-labeled complexes (**8a–8d**) in 100 μL saline solution via the tail vein. At 2-, 60-, 240-min postinjection, mice were euthanized by cervical dislocation (n = 3/time point), and selected organs were collected, weighed, and counted on a gamma counter containing a NaI crystal. The data were corrected for radioactive decay and percent injected dose per gram (%ID/g) of tissue was calculated. All samples were calibrated against a known standard.

PET/CT Imaging Studies. Small-animal PET/CT imaging studies were conducted in 5xFAD and WT mice weighing 35.1 ± 5.5 g. The mice were administrated with 2.92–3.29 MBq (79–89 μCi) of ^{64}Cu-labeled complexes (**8b** and **8d**) in 100 μL saline solution via tail vein injection. Thus, given that the total volume of blood is ∼2.5 mL for an average size mouse, we predict that the higher limit for the plasma concentration of the injected compounds will be ∼6 μM (150 μM × 0.1 mL/2.5 mL). Mice were anesthetized with 1–2% isofluorane/oxygen and imaged on an Inveon small-animal PET/CT scanner (Siemens Medical Solutions) for 30 min. Dynamic images were collected and reconstructed with the maximum a posteriory probability algorithm followed by CT in coregistration with the Inveon Research Workstation image display software (Siemens Medical Solutions). Regions of interest were selected from PET images with the CT anatomical guidelines, and the associated radioactivity was measured using Inveon Research Workstation software and the brain uptake values were reported at [(nCi/mL)]]/[injected dose (nCi)] without normalizing to body weight. Immediately after dynamic PET/CT scanning, the mice were euthanized, and the selected organs were collected for biodistribution studies. After post-PET biodistribution analysis, the unfixed brains were sectioned sagittally into six thick slices and exposed to a phosphor imaging screen plate for autoradiography.

Statistical Analysis. Data were processed by Origin Lab and presented as mean ± SD. Statistical analysis was performed using one-way ANOVA and Student's t test. Differences at the 95% confidence level ($P < 0.05$) were considered statistically significant.

Data Availability. All study data are included in the article and *SI Appendix*.

ACKNOWLEDGMENTS. We thank Jalen Scott for generating an initial version of Fig. 3*A*. This work was supported by research funding from the NIH (Grant R01GM114588 to L.M.M.), Washington University Knight Alzheimer's Disease Research Center (Pilot Award NIH P50AG05681), and the McDonnell Center for Cellular and Molecular Neurobiology at Washington University School of Medicine for a postdoctoral fellowship to H.-J.C. The PET imaging and biodistribution studies were conducted at the Malinckrodt Institute of Radiology Preclinical Imaging Facility of the Washington University School of Medicine.

1. J. Hardy, D. J. Selkoe, The amyloid hypothesis of Alzheimer's disease: Progress and problems on the road to therapeutics. *Science* **297**, 353–356 (2002).
2. E. Karran, M. Mercken, B. De Strooper, The amyloid cascade hypothesis for Alzheimer's disease: An appraisal for the development of therapeutics. *Nat. Rev. Drug Discov.* **10**, 698–712 (2011).
3. C. Haass, D. J. Selkoe, Soluble protein oligomers in neurodegeneration: Lessons from the Alzheimer's amyloid β-peptide. *Nat. Rev. Mol. Cell Biol.* **8**, 101–112 (2007).
4. I. Benilova, E. Karran, B. De Strooper, The toxic Aβ oligomer and Alzheimer's disease: An emperor in need of clothes. *Nat. Neurosci.* **15**, 349–357 (2012).
5. E. N. Cline, M. A. Bicca, K. L. Viola, W. L. Klein, The Amyloid-β oligomer hypothesis: Beginning of the third decade. *J. Alzheimers Dis.* **64**, S567–S610 (2018).
6. S. S. Hwang *et al.*, Detection of amyloid β oligomers toward early diagnosis of Alzheimer's disease. *Anal. Biochem.* **566**, 40–45 (2019).
7. C. A. Mathis *et al.*, A lipophilic thioflavin-T derivative for positron emission tomography (PET) imaging of amyloid in brain. *Bioorg. Med. Chem. Lett.* **12**, 295–298 (2002).
8. W. E. Klunk *et al.*, Imaging brain amyloid in Alzheimer's disease with Pittsburgh Compound-B. *Ann. Neurol.* **55**, 306–319 (2004).
9. B. T. Hyman, J. Q. Trojanowski, Consensus recommendations for the postmortem diagnosis of Alzheimer disease from the National Institute on Aging and the Reagan Institute working group on diagnostic criteria for the neuropathological assessment of Alzheimer disease. *J. Neuropathol. Exp. Neurol.* **56**, 1095–1097 (1997).
10. R. J. Perrin, A. M. Fagan, D. M. Holtzman, Multimodal techniques for diagnosis and prognosis of Alzheimer's disease. *Nature* **461**, 916–922 (2009).
11. A. Nordberg, PET imaging of amyloid in Alzheimer's disease. *Lancet Neurol.* **3**, 519–527 (2004).
12. A. G. Vlassenko, T. L. S. Benzinger, J. C. Morris, PET amyloid-beta imaging in preclinical Alzheimer's disease. *Biochim. Biophys. Acta* **1822**, 370–379 (2012).
13. D. J. Hayne, S. Lim, P. S. Donnelly, Metal complexes designed to bind to amyloid-β for the diagnosis and treatment of Alzheimer's disease. *Chem. Soc. Rev.* **43**, 6701–6715 (2014).
14. M. Ono, H. Saji, Recent advances in molecular imaging probes for β-Amyloid plaques. *MedChemComm* **6**, 391–402 (2015).
15. A. C. Sedgwick *et al.*, Metal-based imaging agents: Progress towards interrogating neurodegenerative disease. *Chem. Soc. Rev.* **49**, 2886–2915 (2020).
16. P. W. Miller, N. J. Long, R. Vilar, A. D. Gee, Synthesis of ^{11}C, ^{18}F, ^{15}O, and ^{13}N radiolabels for positron emission tomography. *Angew. Chem. Int. Ed. Engl.* **47**, 8998–9033 (2008).
17. T. J. Wadas, E. H. Wong, G. R. Weisman, C. J. Anderson, Coordinating radiometals of copper, gallium, indium, yttrium, and zirconium for PET and SPECT imaging of disease. *Chem. Rev.* **110**, 2858–2902 (2010).
18. C. J. Anderson, R. Ferdani, Copper-64 radiopharmaceuticals for PET imaging of cancer: Advances in preclinical and clinical research. *Cancer Biother. Radiopharm.* **24**, 379–393 (2009).
19. M. Shokeen, C. J. Anderson, Molecular imaging of cancer with copper-64 radiopharmaceuticals and positron emission tomography (PET). *Acc. Chem. Res.* **42**, 832–841 (2009).
20. A. Boschi, P. Martini, E. Janevik-Ivanovska, A. Duatti, The emerging role of copper-64 radiopharmaceuticals as cancer theranostics. *Drug Discov. Today* **23**, 1489–1501 (2018).
21. X. Nie *et al.*, PET/MRI of hypoxic atherosclerosis using ^{64}Cu-ATSM in a rabbit model. *J. Nucl. Med.* **57**, 2006–2011 (2016).
22. J. S. Lewis, D. W. McCarthy, T. J. McCarthy, Y. Fujibayashi, M. J. Welch, Evaluation of 64Cu-ATSM in vitro and in vivo in a hypoxic tumor model. *J. Nucl. Med.* **40**, 177–183 (1999).
23. A. L. Vävere, J. S. Lewis, Cu-ATSM: A radiopharmaceutical for the PET imaging of hypoxia. *Dalton Trans.* **36**, 4893–4902 (2007).
24. K. Chen, M. Cui, Recent progress in the development of metal complexes as β-amyloid imaging probes in the brain. *MedChemComm* **8**, 1393–1407 (2017).
25. J. L. Hickey, P. S. Donnelly, Diagnostic imaging of Alzheimer's disease with copper and technetium complexes. *Coord. Chem. Rev.* **256**, 2367–2380 (2012).
26. J. L. Hickey *et al.*, Diagnostic imaging agents for Alzheimer's disease: Copper radiopharmaceuticals that target Aβ plaques. *J. Am. Chem. Soc.* **135**, 16120–16132 (2013).
27. L. E. McInnes *et al.*, Potential diagnostic imaging of Alzheimer's disease with copper-64 complexes that bind to amyloid-β plaques. *Inorg. Chem.* **58**, 3382–3395 (2019).
28. M. T. Fodero-Tavoletti *et al.*, Bis(thiosemicarbazonato) Cu-64 complexes for positron emission tomography imaging of Alzheimer's disease. *J. Alzheimers Dis.* **20**, 49–55 (2010).
29. A. K. Sharma *et al.*, Bifunctional compounds for controlling metal-mediated aggregation of the $a\beta_{42}$ peptide. *J. Am. Chem. Soc.* **134**, 6625–6636 (2012).
30. A. K. Sharma *et al.*, Small bifunctional chelators that do not disaggregate amyloid β fibrils exhibit reduced cellular toxicity. *Inorg. Chem.* **53**, 11367–11376 (2014).
31. N. Bandara *et al.*, Evaluation of ^{64}Cu-based radiopharmaceuticals that target Aβ peptide aggregates as diagnostic tools for Alzheimer's disease. *J. Am. Chem. Soc.* **139**, 12550–12558 (2017).
32. A. K. Sharma, J. W. Schultz, J. T. Prior, N. P. Rath, L. M. Mirica, Coordination chemistry of bifunctional chemical agents designed for applications in ^{64}Cu PET imaging for Alzheimer's disease. *Inorg. Chem.* **56**, 13801–13814 (2017).
33. H.-J. Cho, A. K. Sharma, Y. Zhang, M. L. Gross, L. M. Mirica, A multifunctional chemical agent as an attenuator of amyloid burden and neuroinflammation in Alzheimer's disease. *ACS Chem. Neurosci.* **11**, 1471–1481 (2020).
34. L. Mirica, A. Sharma, J. Schultz, "Metal-binding bifunctional compounds as diagnostic agents for Alzheimer's disease." US Patent 9,422,286 B2 (2016).
35. M. Mammen, S.-K. Choi, G. M. Whitesides, Polyvalent interactions in biological systems: Implications for design and use of multivalent ligands and inhibitors. *Angew. Chem. Int. Ed. Engl.* **37**, 2754–2794 (1998).
36. Z.-B. Li, K. Chen, X. Chen, (68)Ga-labeled multimeric RGD peptides for microPET imaging of integrin α(v)β ($_3$) expression. *Eur. J. Nucl. Med. Mol. Imaging* **35**, 1100–1108 (2008).
37. W. Liu *et al.*, Imparting multivalency to a bifunctional chelator: A scaffold design for targeted PET imaging probes. *Angew. Chem. Int. Ed. Engl.* **48**, 7346–7349 (2009).

Downloaded at Palestinian Territory, occupied on November 23, 2021
www.manaraa.com

38. V. M. Krishnamurthy, V. Semetey, P. J. Bracher, N. Shen, G. M. Whitesides, Dependence of effective molarity on linker length for an intramolecular protein-ligand system. *J. Am. Chem. Soc.* **129**, 1312–1320 (2007).
39. H. F. Kung, S. R. Choi, W. Qu, W. Zhang, D. Skovronsky, 18F stilbenes and styrylpyridines for PET imaging of A β plaques in Alzheimer's disease: A miniperspective. *J. Med. Chem.* **53**, 933–941 (2010).
40. M. Ono *et al*., Synthesis and evaluation of novel chalcone derivatives with (99m)Tc/Re complexes as potential probes for detection of β-amyloid plaques. *ACS Chem. Neurosci.* **1**, 598–607 (2010).
41. X. Zhang *et al*., ^{99m}Tc-Labeled 2-Arylbenzothiazoles: Aβ imaging probes with favorable brain pharmacokinetics for single-photon emission computed tomography. *Bioconjug. Chem.* **27**, 2493–2504 (2016).
42. T. M. Siclovan *et al*., "Agents for imaging soluble A-Beta." US Patent 7,727,511 B2 (2010).
43. S. Ait-Mohand *et al*., Evaluation of ^{64}Cu-labeled bifunctional chelate-bombesin conjugates. *Bioconjug. Chem.* **22**, 1729–1735 (2011).
44. M. S. Cooper *et al*., Comparison of (64)Cu-complexing bifunctional chelators for radioimmunoconjugation: Labeling efficiency, specific activity, and in vitro/in vivo stability. *Bioconjug. Chem.* **23**, 1029–1039 (2012).
45. V. Zinchuk, Y. Wu, O. Grossenbacher-Zinchuk, Bridging the gap between qualitative and quantitative colocalization results in fluorescence microscopy studies. *Sci. Rep.* **3**, 1365 (2013).
46. S. K. Bhal, K. Kassam, I. G. Peirson, G. M. Pearl, The rule of five revisited: Applying log D in place of log P in drug-likeness filters. *Mol. Pharm.* **4**, 556–560 (2007).
47. T. T. Wager *et al*., Defining desirable central nervous system drug space through the alignment of molecular properties, in vitro ADME, and safety attributes. *ACS Chem. Neurosci.* **1**, 420–434 (2010).
48. M. Kume *et al*., A semi-automated system for the routine production of copper-64. *Appl. Radiat. Isot.* **70**, 1803–1806 (2012).
49. D. W. McCarthy *et al*., Efficient production of high specific activity ^{64}Cu using a biomedical cyclotron. *Nucl. Med. Biol.* **24**, 35–43 (1997).

Downloaded at Palestinian Territory, occupied on November 23, 2021

www.manaraa.com